U-Shaped Spectrograms Registered by the DEMETER Satellite: Observational Features and Formation Mechanism

D. Shklyar, Michel Parrot, E. E Titova

Key Points:
- U-shaped spectrum registered in the equatorial region of the upper ionosphere during nighttime is formed by lightning-induced whistler waves
- Latitudinal dependence of the upper cutoff frequency is determined by the peculiarities of oblique wave propagation and attenuation
- The wave attenuation can be calculated along the trajectories found from the equations of geometrical optics that disregard collisions

Correspondence to:
D. R. Shklyar,
david@iki.rssi.ru

U-Shaped Spectrograms Registered by the DEMETER Satellite: Observational Features and Formation Mechanism

D. R. Shklyar[1,2] ID **, M. Parrot[3]** ID **, and E. E. Titova[1,4]**

[1]Space Research Institute, Russian Academy of Sciences, Moscow, Russia, [2]National Research University Higher School of Economics, Moscow, Russia, [3]LPC2E/CNRS, Orléans, France, [4]Polar Geophysical Institute, Apatity, Russia

Abstract U-shaped spectrograms observed by the DEMETER satellite in the equatorial region of the upper ionosphere are presented and explained for the first time. These spectra are characterized by the latitude-dependent upper cutoff frequency that increases with the latitude during nighttime. The observations suggest that this very low frequency wave phenomenon is closely connected with the anomalous increase in cold plasma density at and below the satellite. We show that restricting the analysis to propagation effects is insufficient to explain U-shaped spectra, and other effects, in particular, the collisional wave damping should be taken into consideration. To calculate the wave damping, we use the method of successive approximations. In the first approximation, we calculate the ray trajectory and the wave normal vector along it, using the equations of geometrical optics neglecting collisions. In the second approximation we calculate the collisional wave damping along the precalculated trajectory. We show that the effects of very low frequency wave propagation and attenuation in the equatorial region of the upper ionosphere explain the main features of the phenomenon under discussion.

1. Introduction

The DEMETER satellite, which operated in the orbit for more than 6 years, was very successful in observing various very low frequency (VLF) wave phenomena, both known before and yet unknown. Its payload measured electromagnetic waves in different frequency ranges from ultralow frequency to medium frequency, and also plasma parameters such as the ion density given by the ion analyzer IAP (Berthelier, Godefroy, Leblanc, Seran, et al., 2006). The VLF electric spectrograms up to 20 kHz were always on board calculated with a low time (2 s) and frequency (19 Hz) resolution all around the Earth except in the auroral zone (Berthelier, Godefroy, Leblanc, Malingre, et al., 2006). Along with familiar ion cyclotron and electron whistlers induced by lightning strokes (Gurnett et al., 1965; Helliwell, 1965; Smith et al., 1964; Storey, 1953), the observations include magnetospheric line radiation (Němec et al., 2009), wedge-like spectra (Shklyar et al., 2010), the first time registered ionospherically reflected proton whistlers (Vavilov & Shklyar, 2014), and many others. The variety of unusual VLF wave events have been collected and presented in the review paper by Parrot et al. (2015).

In the present article we study U-shaped spectrograms, the VLF wave phenomenon observed sometimes by DEMETER in the equatorial region of the orbit, which has not yet been completely understood. Figure 1 shows an example of spectrogram under discussion that clarifies the appellation of this wave phenomenon. In the next section, we present more examples of U-shaped spectra which reveal close relation of these wave events to the increase in the ambient plasma density. The key points in the approach that we use to explain U-shaped spectra are given in section 3. VLF wave propagation in the equatorial region of the ionosphere is described in section 4. The features of collisional wave absorption in the ionosphere that give the key to understanding U-shaped spectra are discussed in section 5. Finally, the results of the paper are summarized in section 6.

2. Observational Features of U-Shaped Spectrograms

Further examples of U-shaped spectra are shown in Figures 2–4. The details of electromagnetic field measurements and data processing on board DEMETER can be found in Berthelier, Godefroy, Leblanc, Malingre, et al. (2006). The data beneath each spectrum display orbital parameters, of which the geomagnetic latitude is the most important in the present context. We should recall that the orbit of DEMETER was circular and was lowered from 700 km to 660 km in December 2005. Thus, all the measurements discussed in the present paper were taken at the altitude of 660 km. We see that the upper cutoff frequencies in the spectra are almost
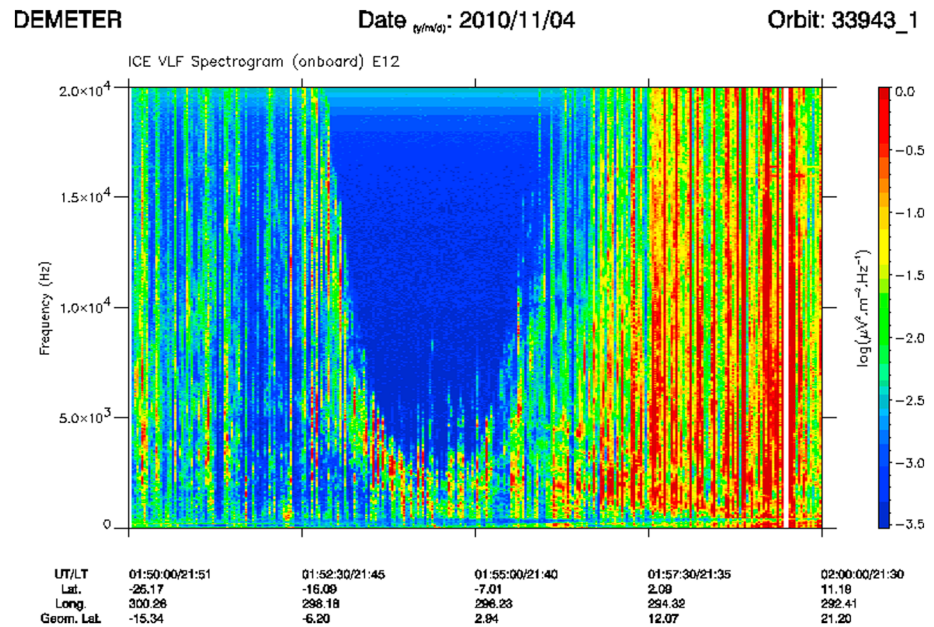
Figure 1. An example of U-shaped spectrogram registered by DEMETER in the equatorial region of the upper ionosphere. It corresponds to data recorded on 4 November 2010 between 01:50:00 and 02:00:00 UT. The frequency range is up to 20 kHz. The intensity is color coded according to the color scale on the right. In the bottom, the geographic latitude and longitude are indicated together with the geomagnetic latitude. Each vertical line is a fractional-hop whistler, which corresponds to a lightning stroke in the atmosphere (see section 3). DEMETER = Detection of Electro-Magnetic Emissions Transmitted from Earthquake Regions; VLF = very low frequency.

symmetrical with respect to the equator, although this property is by no means strict. The variation of plasma density shown below each spectrum indicates clearly that U-shaped spectrum is connected with the unusual increase in plasma density registered on the satellite. The relation of U-shaped spectrum to an enhanced plasma density is further illustrated by Figure 5, which displays the spectrogram taken under conditions of lower plasma density. We see that in this case the U shape on the spectrogram is less pronounced than that in the cases of larger plasma density shown above.

We should mention one important point concerning plasma density measurements. At DEMETER altitudes, O^+ are the dominant ions. Thus, the electron density, which essentially determines the wave attenuation, is very close to O^+ density displayed in the figures.

Figures 3 and 4 aim to illustrate that the width of the U-shaped spectrum increases with increasing plasma density. Another important characteristic of U-shaped spectrum is the minimum cutoff frequency in the spectrum registered at or close to the equator, which we denote by f_{cmin}. While the notion of minimum cutoff frequency is self-evident, the definition of cutoff frequency itself needs to be clarified. By cutoff frequency we understand the frequency at which the spectral intensity merges with the noise level. The minimum cutoff frequency is determined by many factors, of course, but the plasma density seems to be the key one. In general, the quantity f_{cmin} decrease with increasing plasma density. Figure 6 illustrates the dependence of the maximum latitudinal width at the 20-kHz level of the U shape and the minimum cutoff frequency in the spectrum on the equatorial plasma density measured by DEMETER.

We will note another important peculiarity of the wave phenomenon under discussion. As one can notice from the examples of U-shaped spectra shown above, if plasma density on one side of the equator is substantially large, then the spectrum has a sharp cutoff frequency with a distinct dependence on the latitude, while when the density is not that large the cutoff frequency is somewhat vague.

As was pointed out by one of the reviewers, the U-shaped spectra shown in Figures 1–4 had all been taken at geographic latitudes near 300°, where the geomagnetic field strength at the equator is strongest as compared to the dipole value. We do not have a clear explanation for this observational feature. We suppose that the preferable observation of these events near 300° geographic longitude may be related to statistically significant enhancement of the electron density in this region that has previously been shown in Figure 6 of
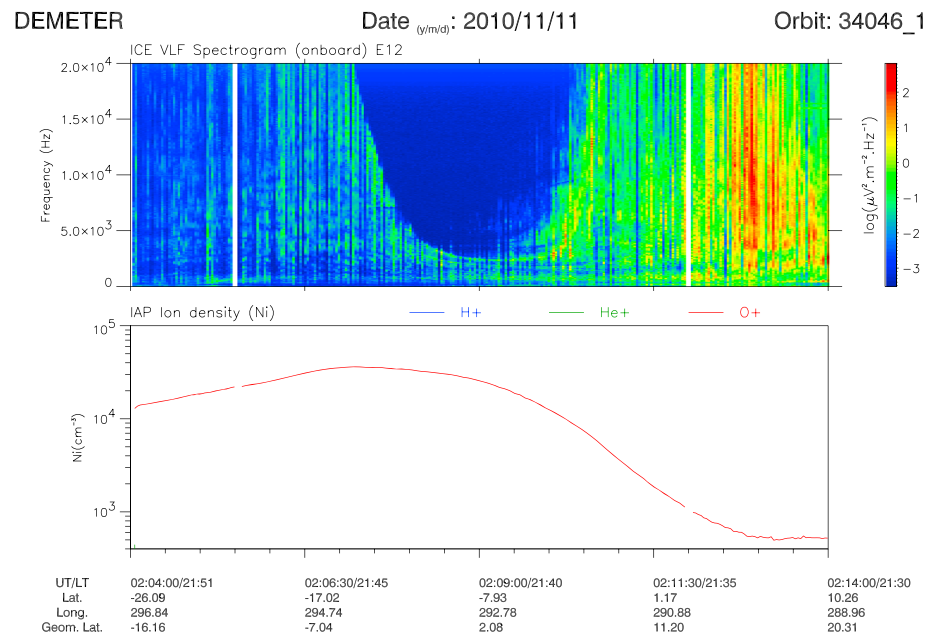
Figure 2. (upper panel) Similar to Figure 1 but it corresponds to data recorded on 11 November 2010 between 02:04:00 and 02:14:00 UT. (lower panel) Corresponding ion density recorded by the IAP experiment. At the DEMETER altitude the ion O+ is preponderant. DEMETER = Detection of Electro-Magnetic Emissions Transmitted from Earthquake Regions; VLF = very low frequency.

Parrot et al. (2009). We are now checking all the nighttime half orbits of DEMETER (more than 30,000 orbits) in order to obtain a statistic, and we intend to present the results in a future publication.

3. General Approach to the Explanation of U-Shaped Spectra

As can be inferred from the analysis of spectrograms presented above, the emission observed at the latitudes adjacent to the U-shaped spectrum is nothing but sferics originating from lightnings. Thus, our first assumption is that U-shaped spectrum is formed by lightning-induced emission. This emission first propagates in the
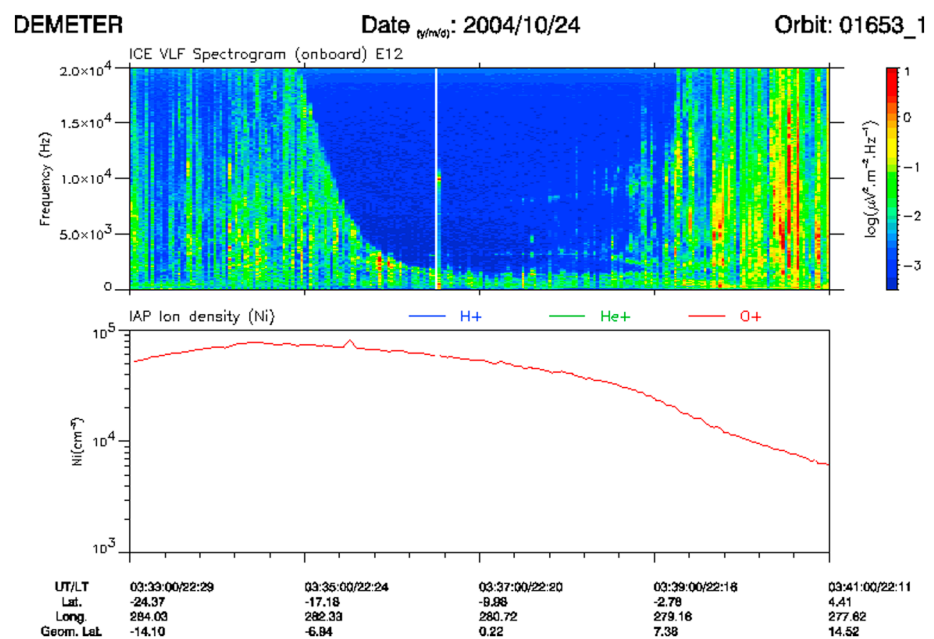

Figure 3. Similar to Figure 2 but for data recorded on 24 October 2004 between 03:33:00 and 03:41:00 UT.
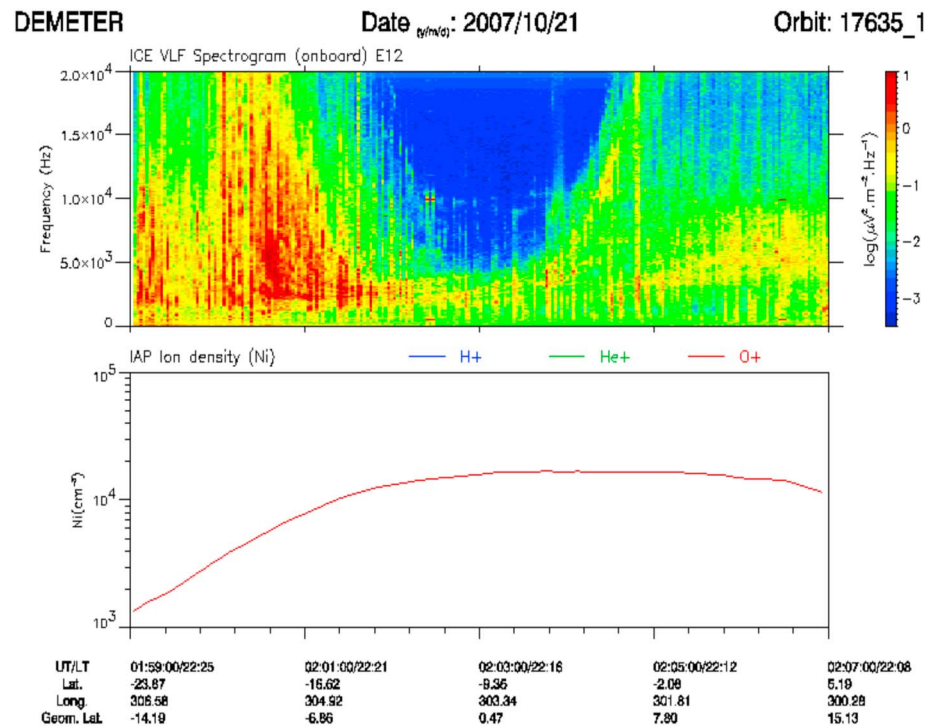
Figure 4. Similar to Figure 2 but for data recorded on 21 October 2007 between 01:59:00 and 02:07:00 UT.

Earth-ionosphere wave guide, partly leaking through the lower to upper ionosphere. Due to refraction property of the ionosphere in which the propagation speed there is much lower than that in the atmosphere, shortly after a lightning stroke the emission is localized in a thin horizontal layer of the ionosphere. This layer is centered on the latitude of the lightning stroke, of course, but has a finite width over latitude. Basing on experimental data, Vavilov and Shklyar (2014) estimated this width to be on the order of 40° (or ~4,000 km) in total. We will take this configuration as the initial condition for the electromagnetic field when considering the evolution of the wave field after the lightning stroke. Spatial Fourier transform of this field
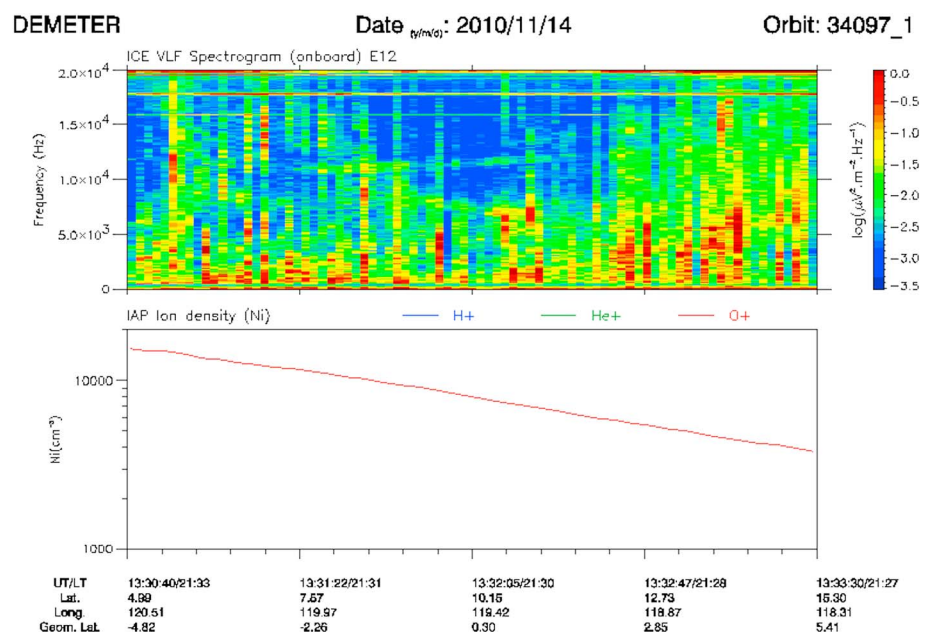

Figure 5. Similar to Figure 2 but for data recorded on 14 November 2010 between 13:30:40 and 13:33:30 UT when the plasma density was low as compared to the cases shown in Figures 2 to 4.
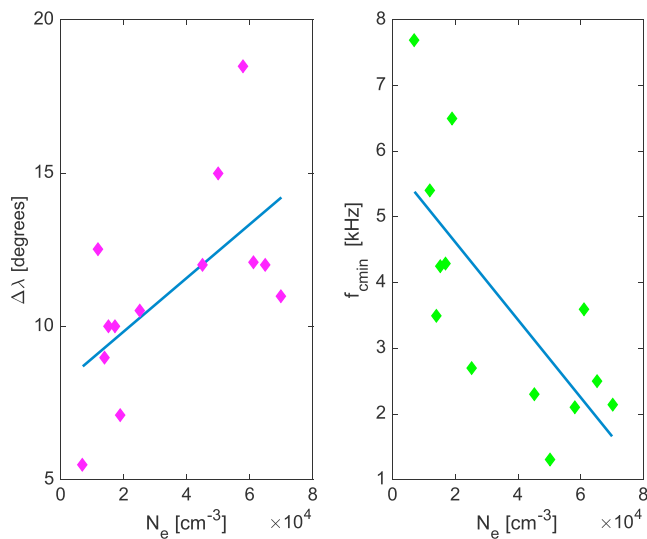
Figure 6. (left) Latitudinal width of U-shaped measured at 20-kHz level. (Right) Minimum cutoff frequency in the spectrum that appears at or close to the equator. Both quantities are presented as the function of equatorial plasma density measured on board the satellite. The measured quantities are shown by diamond signs. The straight lines are linear fits to the data.

will be dominated by the wave vectors with vertical components much larger than horizontal ones, that is, the wave vectors directed almost vertically. Each wave vector in this expansion gives rise to a wave packet with the frequency determined by the local dispersion relation, which is then conserved along the ray trajectory of the given wave packet.

We will be interested in the frequency range of observation, that is, 1–20 kHz, which in the upper ionosphere corresponds to the lower part of whistler mode band. For such waves, the wave length λ is of the order of $(c/f_p)(f_c/f)^{1/2}$, where $f_p = \omega_p/2\pi$, $f_c = \omega_c/2\pi$ are electron plasma and cyclotron frequencies, respectively, $f = \omega/2\pi$ is the wave frequency, and c is the speed of light. Using typical ionospheric plasma parameters one can show that at the altitudes of 120 km and higher, the wave length is much smaller than the scale of inhomogeneity $\mathcal{L}$, that is, $\lambda \ll \mathcal{L}$. Hence, our second assumption is that above 120 km the trajectories of the wave packets that form U-shaped spectrum are well described by the equations of geometrical optics (GO).

As will be shown below (see section 4), U-shaped spectrum cannot be explained solely by propagation effects, and other factors should be taken into consideration. We suppose that collisional wave damping plays a crucial role in formation of the observed spectrum. Our main assumption consists in that the wave damping can be accurately taken into account by the method of successive approximations, which permits to divide the wave propagation and attenuation. Specifically, we solve the equations of GO in nonabsorptive plasma, that is, neglecting collisions. These equations define the ray trajectory, as well as the wave normal vector along it. Then, one can substitute the obtained wave normal vector and also the plasma parameters along the ray trajectory, into general dispersion relation with the account of collisions and find complex wave frequency that takes into account the wave
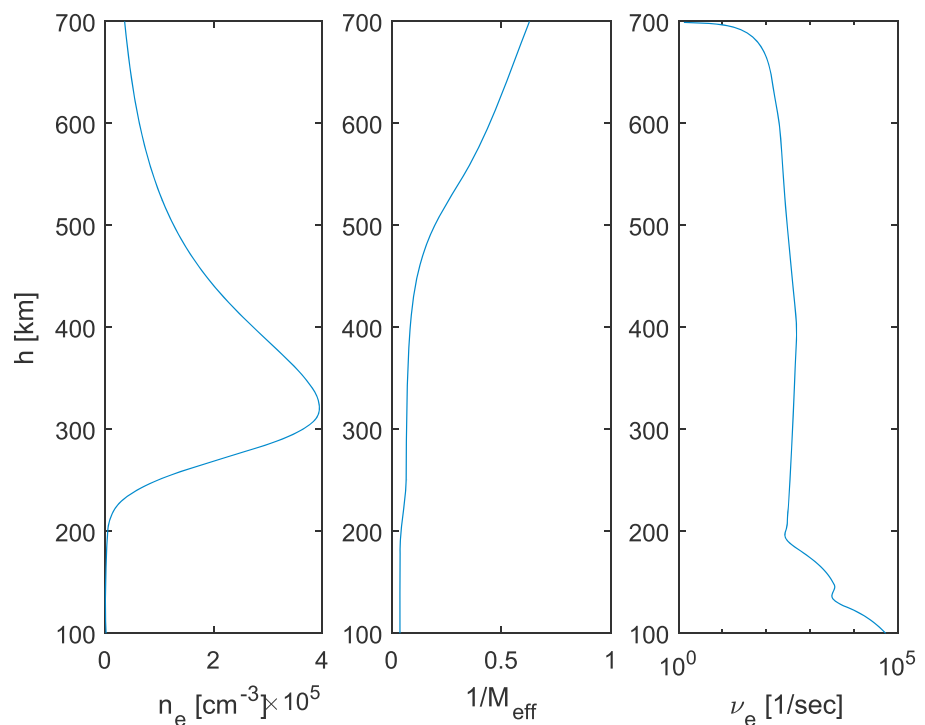

Figure 7. Height profiles of the electron density (left panel), the inverse effective ion mass (middle panel), and electron collision frequency (right panel) used in calculations. The data inferred from the IRI-2016 model correspond to 1 January 2010, 22:00 LT, Latitude= 5°, Longitude = 40°.
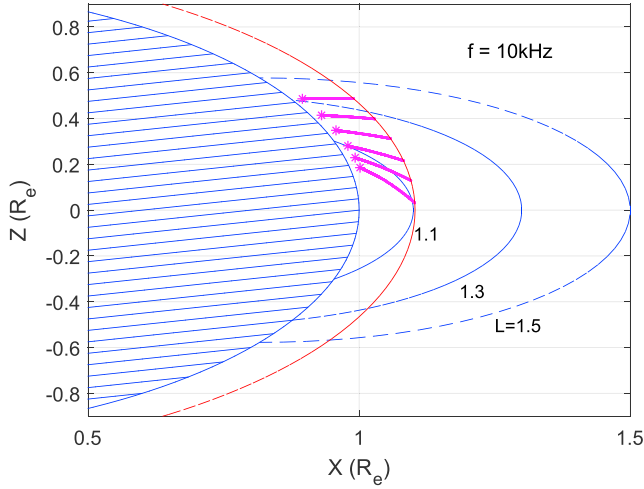
Figure 8. Trajectories of 10-kHz wave packets that, along with other frequency wave packets, form U-shaped spectrum. Geomagnetic field lines corresponding to the values of MacIlwain parameter $L = 1.1$, 1.3, and 1.5 are shown by blue dashed lines. DEMETER orbit is shown by red dashed line. Parameters of the six trajectories are given in Table 1.

attenuation. Alternatively, one can substitute real frequency and all, but one, real components of the wave normal vector and find the remaining complex component that describes spatial wave attenuation. Due to the reasons explained below, we will further use the second possibility. We now turn to the solution of GO equations.

4. VLF Wave Propagation in the Equatorial Region of the Ionosphere

As has been mentioned above, in the Earth's ionosphere the frequency range under discussion corresponds to whistler mode waves. The feature of wave propagation in the equatorial region is such that the waves have large wave normal angles close (but not equal!) to $\pi/2$. We will underline that we assume nonducted propagation for fractional-hop whistlers that form the U-shaped spectrum. Another peculiarity is a substantial variation of the parameter f_p/f_c over the altitude range of interest, namely, from 120 km where we start our calculations to ~ 660 km, that is, the altitude of observation on DEMETER. The dispersion relation for whistler mode waves having large wave normal angle, which is valid for arbitrary ratio f_p/f_c, has been obtained by Shklyar et al. (2017) and has the form

$$\omega^2 = \omega_{LH}^2 \frac{k^2}{k^2 + q^2 \frac{\omega_p^2}{\omega_{UH}^2}} + \frac{\omega_p^2 \omega_c^2}{\omega_{UH}^2} \frac{k_\parallel^2 k^2}{(k^2 + q^2)\left(k^2 + q^2 \frac{\omega_p^2}{\omega_{UH}^2}\right)} \,, \quad (1)$$

where $\omega_{UH} = \sqrt{\omega_p^2 + \omega_c^2}$ is the upper hybrid frequency, $k_\parallel$ and k are the parallel component and the magnitude of the wave normal vector, respectively, and the quantities q and the lower hybrid resonance frequency ω_{LH} are determined by the following relations:

$$q^2 = \frac{\omega_p^2}{c^2} \;; \quad \omega_{LH}^2 = \frac{1}{M_{eff}} \frac{\omega_{pi}^2 \omega_c^2}{\omega_{UH}^2} \,.$$

Here ω_{pi} is the proton plasma frequency and M_{eff} is the effective ion mass normalized to the proton mass.

When solving 2-D GO equations based on the dispersion relation (1), we will use the dipolar model of the ambient magnetic field. As for plasma density and the effective ion mass, we will assume these quantities to depend only on the height, neglecting their dependence on latitude. The corresponding profiles used in calculations are shown in Figure 7. The data are obtained from IRI 2016 model and correspond to 1 January 2010, 22:00 LT, geomagnetic latitude 5° and longitude 40°. The right panel shows the profile of electron collision frequency, which is used in section 5 for estimation of wave attenuation. The ray trajectories for 10 kHz wave packets starting at various latitudes at the height of 120 km and reaching the satellite at the height of 660 km are shown in Figure 8. All wave packets have vertical direction of the initial wave normal vector. Initial and final latitudes, as well as initial and final wave normal angles corresponding to the trajectories shown in Figure 8 are given in Table 1. The trajectories are numbered in the order of increasing initial latitude.

Table 1
Initial and Final Parameters of the Six Trajectories Shown in Figure 8

Parameter	Trajectory #					
	Traj. 1	Traj. 2	Traj. 3	Traj. 4	Traj. 5	Traj. 6
$\lambda_0 =$	10.5°	13.0°	16.0°	20.0°	24.0°	28.5°
$\lambda_f =$	1.6°	6.7°	11.3°	16.4°	21.2°	26.2°
$\theta_0 =$	69.7°	65.2°	60.2°	53.9°	48.3°	42.6°
$\theta_f =$	51.8°	56.3°	54.0°	49.1°	44.1°	38.9°

Trajectories of wave packets in the whole frequency band from 1 to 20 kHz show similar behavior. We see that some trajectories come to the equatorial region; thus, all wave frequencies would be registered there provided that the corresponding wave packets had sufficiently large amplitudes. This is confirmed by Figures 1 – 4 where it can be seen that the whistlers have a small dispersion and, thus, are coming from an area not very far below the satellite.

5. Collisional Wave Absorption in the Ionosphere

5.1. Temporal Versus Spatial Attenuation of a Wave Packet

As it is clear from the above consideration, the problem of wave packet damping is the initial value problem. The initial amplitude of the wave packet, apart from the intensity of lightning stroke, depends at least on frequency and the distance between the lightning and the exit point of the wave packet into ionosphere (Fiser et al., 2010). Discussion of this dependence is far beyond the scope of the present study, thus, we will only keep this factor in mind.

The net attenuation of the wave packet is given by the integral

$$\Gamma = \int_{t_0}^{t_s} \gamma(t) dt , \tag{2}$$

where γ is the imaginary part of the wave frequency, so that the complex frequency $\Omega = \omega + i\gamma$. The integral in (2) is taken between some initial time t_0 and the time of wave packet arrival at the satellite. Let us show that, as far as the wave attenuation is concerned, this nonstationary problem with initial conditions can be reduced to the solution of a stationary problem for a monochromatic wave. More specifically, calculation of the integral (2) can be reduced to the calculation of the integral of imaginary part of the vertical component of the wave normal vector over the height. Namely, let us show that

$$\int_{t_0}^{t_s} \gamma(t) dt = - \int_{h_0}^{h_s} Im\{k_h(h)\} dh . \tag{3}$$

(Here and further, for all vectors concerned, we denote their radial components by index h and horizontal components by index λ). Indeed, the quantity γ is determined from the dispersion relation that can generally be written in the form

$$F(k_h, k_\lambda, \Omega) + iG(k_h, k_\lambda, \Omega) = 0 , \tag{4}$$

the inequality $|G(k_h, k_\lambda, \Omega)| \ll |F(k_h, k_\lambda, \Omega)|$ being fulfilled in the case of weak damping that we assume. Then, for real k_h, k_λ, the quantity γ is determined by the relation

$$\gamma = - \frac{G(k_h, k_\lambda, \omega)}{\partial F / \partial \omega} . \tag{5}$$

On the other hand, for real Ω and k_λ, the imaginary part of the wave vector component k_h is given by

$$Im\{k_h\} = - \frac{G(Re\{k_h\}, k_\lambda, \omega)}{\partial F / \partial k_h} . \tag{6}$$

Taking into account that the vertical component of the group velocity is equal to

$$V_{g_h} = - \frac{\partial F}{\partial k_h} / \frac{\partial F}{\partial \omega} ,$$

and that $dt = dh/V_{g_h}$, from (5) and (6) we get the required relation (3).

5.2. Equations for the Wave Field

The expressions for real wave components of a monochromatic wave can be written in the following form:

$$\mathcal{E}(\mathbf{r}, t) = Re \left\{ \mathbf{E}_0(\mathbf{r}) e^{-i\omega t} \right\} , \quad \mathcal{B}(\mathbf{r}, t) = Re \left\{ \mathbf{B}_0(\mathbf{r}) e^{-i\omega t} \right\} . \tag{7}$$

Equations for the quantities $\mathbf{E}_0(\mathbf{r})$ and $\mathbf{B}_0(\mathbf{r})$ which follow from Maxwell's equations then read

$$curl\ \mathbf{E}_0 = \frac{i\omega}{c} \mathbf{B_0} ; \quad curl\ \mathbf{B}_0 = -\frac{i\omega}{c} \hat{\varepsilon} \mathbf{E}_0 , \tag{8}$$

where $\hat{\varepsilon}$ is the dielectric tensor.

Equations (8) have the same form in any coordinate system. When solving the GO equations, we used the dipole coordinate system (L, Y, M), with the M axis directed along the ambient magnetic field, L being the orthogonal to M coordinate in the meridional plane, and Y denoting the azimuthal coordinate. This coordinate system is convenient for this purpose since the corresponding dispersion relation contains $k_\parallel$, that is, the wave vector component along the ambient magnetic field. When dealing with the equations for the wave field (8), we will assume that the plasma density and the collision frequency depend only on the height h above the Earth, or, which is the same, on the radial distance from the Earth's center $r = R_E + h$, where R_E is the Earth's radius. Then it is more convenient to use the orthogonal coordinate system $(\lambda, y = Y, r)$, where λ is the latitude. The components of vector $\mathbf{E}_0$ in two coordinate systems are related by

$$E_{0\mu} = U_{\mu j} E_{0j} \; ; \;\; (\mu = \lambda, y, r \; ; \; j = L, Y, M), \tag{9}$$

Here and further we use indices i, j to denote vector and matrix components in the coordinate system (L, Y, M) and indices μ, ν for the coordinate system (λ, y, r). The unitary matrix U is given by

$$U_{\mu j} = \begin{pmatrix} \cos\alpha & 0 & \sin\alpha \\ 0 & 1 & 0 \\ -\sin\alpha & 0 & \cos\alpha \end{pmatrix}, \tag{10}$$

where α is the angle between the local direction of the ambient magnetic field and the vertical (r axis). For dipolar magnetic field, the angle α depends only on the latitude λ and is determined by the equation

$$\tan\alpha = \frac{1}{2\tan\lambda} \; .$$

The relations between the components of all vectors in these coordinate systems has the same form (9), in particular, for the wave magnetic field, wave normal vector, and the radius vector.

In the coordinate system (λ, y, r) equations (8) have the same form, except the change of the dielectric tensor; thus, we get

$$\text{curl } \mathbf{E}_0 = \frac{i\omega}{c} \mathbf{B}_0 \; ; \;\; \text{curl } \mathbf{B}_0 = -\frac{i\omega}{c} \hat{\epsilon} \mathbf{E}_0 \; , \tag{11}$$

where

$$\hat{\epsilon} = U\hat{\epsilon}U^{-1} \; . \tag{12}$$

Relation (12) expresses the dielectric tensor in the coordinate system (λ, y, r) through the dielectric tensor in coordinate system (L, Y, M) in which it has the standard form (see, e.g., Ginzburg & Rukhadze, 1972):

$$\hat{\epsilon}_{ij} = \begin{pmatrix} \epsilon_1 & i\epsilon_2 & 0 \\ -i\epsilon_2 & \epsilon_1 & 0 \\ 0 & 0 & \epsilon_3 \end{pmatrix} \tag{13}$$

Under conditions (below ω_{ci} is the ion cyclotron frequency, ν_e is the electron collision frequency, ν_i is the averaged ion collision frequency)

$$\omega_{ci} \ll \omega \ll \omega_c \; ; \;\; \nu_e^2 \ll \omega_c^2 \tag{14}$$

which are fulfilled in the region under consideration, the components of the dielectric tensor may be written as

$$\epsilon_1 \simeq 1 + \frac{\omega_p^2(\omega + i\nu_e)}{\omega\omega_c^2} - \frac{1}{M_{\text{eff}}} \frac{\omega_{pi}^2}{\omega(\omega + i\nu_i)} \; ;$$

$$\epsilon_2 \simeq -\frac{\omega_p^2}{\omega\omega_c} \; ; \;\; \epsilon_3 = 1 - \frac{\omega_p^2}{\omega(\omega + i\nu_e)} \; . \tag{15}$$

Using (12) and (13) we obtain the dielectric tensor in the coordinate system (λ, y, r)

$$\hat{\epsilon}_{\mu\nu} = \begin{pmatrix} \tilde{\epsilon}_1 & i\epsilon_2\cos\alpha & \tilde{\epsilon}_{31} \\ -i\epsilon_2\cos\alpha & \epsilon_1 & i\epsilon_2\sin\alpha \\ \tilde{\epsilon}_{31} & -i\epsilon_2\sin\alpha & \tilde{\epsilon}_3 \end{pmatrix} \tag{16}$$
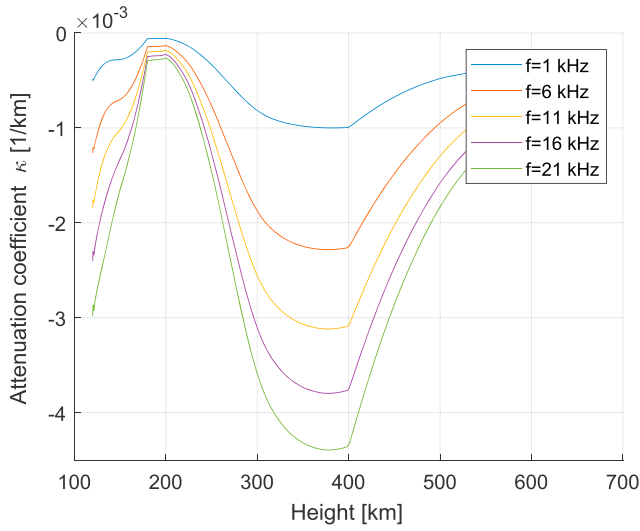
Figure 9. Spatial attenuation coefficient as the function of height for various frequency waves registered at the satellite height, at the latitude of 6°. Total wave attenuation corresponding to frequencies 1, 6, 11, 16, and 21 kHz is equal to 2.4, 5.1, 7.0, 8.5, and 10.0 dB, respectively.

where

$$\tilde{\varepsilon}_1 = \varepsilon_1\cos^2\alpha + \varepsilon_3\sin^2\alpha \;; \quad \tilde{\varepsilon}_{31} = (\varepsilon_3 - \varepsilon_1)\sin\alpha\cos\alpha \;; \quad \tilde{\varepsilon}_3 = \varepsilon_1\sin^2\alpha + \varepsilon_3\cos^2\alpha \;;$$

and the quantities $\varepsilon_1, \varepsilon_2, \varepsilon_3$ are given by (15).

We will look for the solution of equations (11) in the form

$$\mathbf{E}_0(\mathbf{r}) = \mathbf{E}(\mathbf{r})e^{i\Psi(\mathbf{r})} \;; \quad \mathbf{B}_0(\mathbf{r}) = \mathbf{B}(\mathbf{r})e^{i\Psi(\mathbf{r})} \;, \tag{17}$$

assuming $\mathbf{E}(\mathbf{r})$ and $\mathbf{B}(\mathbf{r})$ to be slowly varying functions of $\mathbf{r}$ as compared to $\Psi(\mathbf{r})$. We consider the wave propagation in meridian plane, so that the vector $\mathbf{r}$ has only two components, namely, r_λ and r_h. We should underline that the function $\Psi(\mathbf{r})$ is not assumed to be real, as well as the vectors $\mathbf{E}(\mathbf{r})$ and $\mathbf{B}(\mathbf{r})$, of course . The derivatives of the function $\Psi(\mathbf{r})$ over coordinates give the corresponding components of the complex wave normal vector:

$$k_\lambda(\lambda, r) = \frac{1}{r}\frac{\partial\Psi(\lambda, r)}{\partial\lambda} \;; \quad k_h = \frac{\partial\Psi(\lambda, r)}{\partial r} \;. \tag{18}$$

Substituting (17) and (18) into (11) and neglecting the derivatives of the amplitudes $\mathbf{E}(\mathbf{r})$, $\mathbf{B}(\mathbf{r})$ we obtain

$$k_h E_y = -\frac{\omega}{c}B_\lambda \;; \quad k_h E_\lambda - k_\lambda E_h = \frac{\omega}{c}B_y \;; \quad k_\lambda E_y = \frac{\omega}{c}B_h \;;$$
$$k_h B_y = \frac{\omega}{c}\left(\tilde{\varepsilon}_1 E_\lambda + i\varepsilon_2\cos\alpha E_y + \tilde{\varepsilon}_{31}E_h\right) \;;$$
$$k_h B_\lambda - k_\lambda B_h = \frac{\omega}{c}\left(i\varepsilon_2\cos\alpha E_\lambda - \varepsilon_1 E_y - i\varepsilon_2\sin\alpha E_h\right) \;; \tag{19}$$
$$k_\lambda B_y = -\frac{\omega}{c}(\tilde{\varepsilon}_{31}E_\lambda - i\varepsilon_2\sin\alpha E_y + \tilde{\varepsilon}_3 E_h) \;;$$

The third and the sixth equations in (19) permit to express B_h and E_h through other wave field components, the corresponding relations do not include k_h. Thus, the set of equations (19) can be reduced to four linear algebraic homogeneous equations for the quantities $E_\lambda, E_y, B_\lambda$, and B_y, each equation containing one term proportional to k_h:
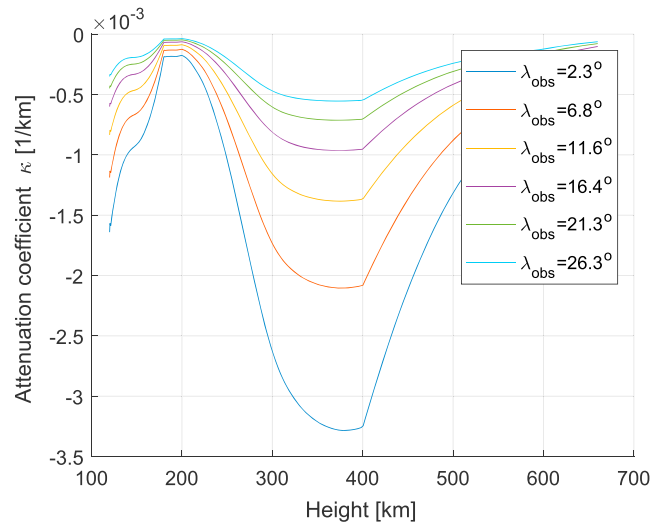

Figure 10. Spatial attenuation coefficient as the function of height for 6-kHz waves registered at various latitudes at the height of 660 km. Total wave attenuation corresponding to the observation latitudes from 2.3° to 26.3° indicated in the insert is equal to 7.1, 4.7, 3.1, 2.2, 1.6, and 1.3 dB, respectively.
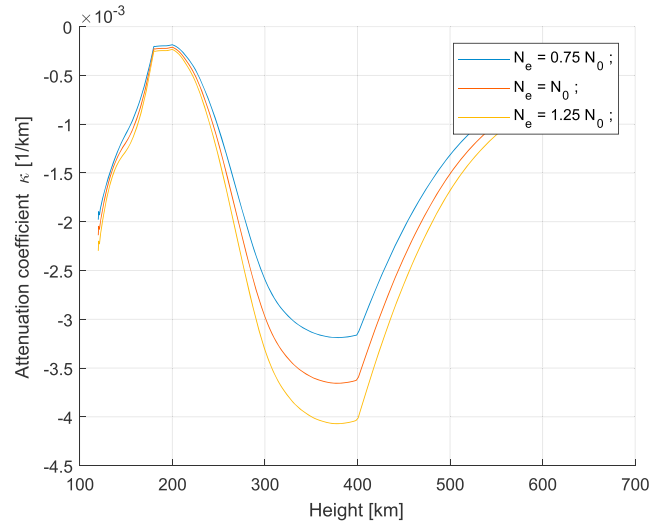
Figure 11. Spatial attenuation coefficient as the function of height for three self-similar profiles of plasma density. The profile $N_0(h)$ is shown in the left panel of Figure 7. Total wave attenuation corresponding to three density profiles indicated in the insert is equal to 7.1, 8.1, and 9.0 dB, respectively.

$$
\begin{aligned}
&k_h E_\lambda = k_\lambda E_h + \frac{\omega}{c} B_y \; ; \\
&k_h E_y = -\frac{\omega}{c} B_\lambda \; ; \\
&k_h B_\lambda = i\frac{\omega}{c}\varepsilon_2 \cos\alpha E_\lambda - \frac{\omega}{c}\left(\varepsilon_1 - \frac{k_\lambda^2 c^2}{\omega^2}\right)E_y - i\frac{\omega}{c}\varepsilon_2 \sin\alpha E_h \; ; \\
&k_h B_y = \frac{\omega}{c}\tilde{\varepsilon}_1 E_\lambda + i\frac{\omega}{c}\varepsilon_2 \cos\alpha E_y + \frac{\omega}{c}\tilde{\varepsilon}_{31} E_h \; ,
\end{aligned}
\tag{20}
$$

where

$$
E_h = -\frac{\left(k_\lambda c/\omega\right)B_y + \tilde{\varepsilon}_{31}E_\lambda - i\varepsilon_2 \sin\alpha E_y}{\tilde{\varepsilon}_3} \; .
\tag{21}
$$

For the sake of compactness, we had not introduced the expression (21) for E_h into the set of equations (20).

The set of equations (20) may be written in matrix form:

$$
k_h \cdot \begin{pmatrix} E_\lambda \\ E_y \\ B_\lambda \\ B_y \end{pmatrix} = \begin{pmatrix} M_{11} & M_{12} & 0 & M_{14} \\ 0 & 0 & M_{23} & 0 \\ M_{31} & M_{32} & 0 & M_{34} \\ M_{41} & M_{42} & 0 & M_{44} \end{pmatrix} \begin{pmatrix} E_\lambda \\ E_y \\ B_\lambda \\ B_y \end{pmatrix}
\tag{22}
$$

with the following expressions for the matrix elements (see (20), (21)):

$$
\begin{aligned}
&M_{11} = -k_\lambda \tilde{\varepsilon}_{31}/\tilde{\varepsilon}_3 \; ; \quad M_{12} = ik_\lambda \varepsilon_2 \sin\alpha/\tilde{\varepsilon}_3 \; ; \quad M_{14} = \left(\omega/c - k_\lambda^2 c/\tilde{\varepsilon}_3\omega\right) \; ; \\
&M_{23} = -\omega/c \; ; \quad M_{31} = i(\omega/c)\varepsilon_2\left(\cos\alpha + \sin\alpha\tilde{\varepsilon}_{31}/\tilde{\varepsilon}_3\right) \; ; \\
&M_{32} = (\omega/c)\left(\varepsilon_2^2 \sin^2\alpha/\tilde{\varepsilon}_3 - \varepsilon_1 + k_\lambda^2 c^2/\omega^2\right) \; ; \quad M_{34} = ik_\lambda \varepsilon_2 \sin\alpha/\tilde{\varepsilon}_3 \; ; \\
&M_{41} = (\omega/c)\left(\tilde{\varepsilon}_1 - \tilde{\varepsilon}_{31}^2/\tilde{\varepsilon}_3\right) \; ; \quad M_{42} = i(\omega/c)\varepsilon_2(\cos\alpha + \tilde{\varepsilon}_{31}\sin\alpha/\tilde{\varepsilon}_3) \; ; \quad M_{44} = -k_\lambda \tilde{\varepsilon}_{31}/\tilde{\varepsilon}_3 \; .
\end{aligned}
$$

We are interested in finding the complex quantity k_h along the wave packet trajectory, remembering that the imaginary part of k_h determines the wave attenuation according to (3). The quantity $-Im\{k_h\}$ is nothing but the wave spatial attenuation coefficient which is denoted by κ in the following figures. Along the wave packet trajectory, all plasma parameters as well as the horizontal component of wave normal vector are known from the solution of GO equations. Thus, solving for the quantity k_h is reduced to eigenvalue problem for known matrix (see (22)), which is solved by standard routine. Since in the frequency band under discussion and in

the absence of collisions there exists only one propagating mode, namely, whistler mode, with the account of collisions there exist only two eigenvalues k_h satisfying the condition

$$|\kappa| \equiv |\text{Im}\left(k_h\right)| \ll |\text{Re}\left(k_h\right)|,$$

and of these two, we are interested in that one having $\text{Re}(kh) > 0$, which corresponds to up-propagating wave. Same as in GO, we neglect the wave reflection in our consideration.

Spatial attenuation coefficient as the function of height along the ray trajectory for 1, 6, 11, 16, and 21 kHz wave packets are shown in Figure 9. All wave packets start at the height of 120 km, at the geomagnetic latitudes 11.95°, 12.41°, 12.59°, 12.75°, and 12.91°, and are registered at the height of 660 km at 5° latitude. We see that for all frequencies the spatial attenuation coefficient has its maximum at the height of about 400 km, that is, in the region of ionosphere *F* layer maximum. The attenuation coefficient increases with frequency, which leads to the appearance of upper cutoff frequency in the observed spectrum.

Figure 10 shows the dependence of the spatial attenuation coefficient on the height, for 6-kHz waves observed at various latitudes. All waves start at 120-km altitude at the latitudes $\lambda_0 = 10.6°$, 12.9°, 16.1°, 19.9°, 24.1° and 28.5°, and come to 660 km at the latitudes indicated in the figure, lower initial latitudes corresponding to lower final ones. We see that the waves registered close to the equator have the largest attenuation coefficient, which explains the formation of U-shaped spectrum.

The dependence of the attenuation coefficient on plasma density is illustrated by Figure 11. The attenuation coefficient as the function of height is calculated for 12-kHz wave, starting vertically from the altitude of 120 km, at the latitude $\lambda_0 = 12°$, for three self-similar profiles of plasma density as indicated in the legend and the figure caption. We see that the attenuation coefficient increases with increasing density, which agrees with the observational results. The dependencies of wave attenuation on frequency, latitude of observation, and the plasma density presented above explain the formation of U-shaped spectrum observed experimentally by DEMETER.

6. Summary

In this paper we have presented the observation of U-shaped spectrum registered by the DEMETER satellite in the equatorial region of the upper ionosphere during nighttime, which is characterized by the presence of the upper cutoff frequency that increases with the increase of latitude at both sides of the equator (see Figures 1–4). The mechanism of U-shaped spectrum formation suggested in this paper is based on the following assumptions. The spectrum is formed by lightning-induced emissions in the VLF frequency band from 1 to 20 kHz, which propagate from the illuminated region of the Earth-ionosphere waveguide to the observation heights (∼700 km) in the whistler mode. The formation of U-shaped spectrum is ascribed to the features of whistler mode wave propagation and collisional attenuation in the indicated region. Due to refractive properties of the ionosphere, the waves in this region propagate with high wave normal angles. It turns out that collisional attenuation of the waves increases with increasing frequency and decreasing latitude of observation. These two factors lead to the formation of the observed U-shaped spectrum. The suggested mechanism permits to explain the main observational feature of the wave phenomenon under discussion, namely, it was observed only under condition that the plasma density measured on board DEMETER was unusually high. This may be understood as follows. With the increase in plasma density, the wave group velocity decreases, thus, the wave propagates through the attenuation region for a longer time which results in larger wave damping. Alternatively, in the frame of stationary problem, this can be understood as the result of increase in the wave normal vector, both its real and imaginary parts, with the same impact on the net wave attenuation.

While the present study permits to understand the main observational features of the wave phenomenon under discussion, numerical simulation of the U-shaped spectrograms requires additional knowledge of statistical properties of lightnings, such as their spatial and temporal distribution over the globe and spectral distribution of emitted energy in the Earth-ionosphere wave guide as the function of latitude and the distance from the lightning stroke, at the least. Discussion of all these characteristics of lightning-induced emission is beyond the scope of the present paper and will be considered in separate publications.

To summarize the theoretical part of the paper, we will say the following. Our explanation of U-shaped spectrum is based on GO. Traditional GO deals with real rays, and real frequencies and wave normal vectors. At the

same time, in the case of inhomogeneous collisional plasma, the equations of GO have complex right-hand sides and, thus, do not possess real solutions. Thus, finding physically meaningful solution to the problem is not trivial. The approach to this problem suggested in the present paper uses the method of successive approximations, assuming that the electron collision frequency is much smaller than the wave frequency. In the zero approximation, we find real ray trajectory and real wave normal vector along this trajectory neglecting collisions. Then, in the first approximation, we find the imaginary part of the wave normal vector and the wave attenuation with the account of collisions. By implementing this approach, we have found the solution to the problem of formation of U-shaped spectrum observed by DEMETER.

References

Berthelier, J. J., Godefroy, M., Leblanc, F., Malingre, M., Menvielle, M., Lagoutte, D., et al. (2006). ICE, the electric field experiment on DEMETER. *Planetary and Space Science*, *54*(5), 456–471. https://doi.org/10.1016/j.pss.2005.10.016

Berthelier, J. J., Godefroy, M., Leblanc, F., Seran, E., Peschard, D., Gilbert, P., & Artru, J. (2006). IAP, the thermal plasma analyzer on DEMETER. *Planetary and Space Science*, *54*(5), 487–501. https://doi.org/10.1016/j.pss.2005.10.017

Fiser, J., Chum, J., Diendorfer, G., Parrot, M., & Santolik, O. (2010). Whistler intensities above thunderstorms. *Annales de Geophysique*, *28*, 37–46.

Ginzburg, V. L., & Rukhadze, A. A. (1972). *Waves in Magnetoactive Plasma, Handbook of Physics*. Berlin: Springer.

Gurnett, D. A., Shawhan, S. D., Brice, N. M., & Smith, R. L. (1965). Ion cyclotron whistlers. *Journal of Geophysical Research*, *70*(7), 1665–1688.

Helliwell, R. A. (1965). *Whistlers and Related Ionospheric Phenomena*. Stanford, CA: Stanford University Press.

Němec, F., Parrot, M., Santolík, O., Rodger, C. J., Rycroft, M. J., Hayosh, M., et al. (2009). Survey of magnetospheric line radiation events observed by the DEMETER spacecraft. *Journal of Geophysical Research*, *114*, A05203. https://doi.org/10.1029/2008JA014016

Parrot, M., Berthelier, J. J., Blecki, J., Brochot, J. Y., Hobara, Y., Lagoutte, D., et al. (2015). Unexpected very low frequency (VLF) radio events recorded by the ionospheric satellite DEMETER. *Surveys in Geophysics*, *36*(3). https://doi.org/10.1007/s10712-015-9315-5

Parrot, M., Inan, U. S., Lehtinen, N. G., & Pincon, J. L. (2009). Penetration of lightning MF signals to the upper ionosphere over VLF ground-based transmitters. *Journal of Geophysical Research*, *114*, A12318. https://doi.org/10.1029/2009JA014598

Shklyar, D. R., Balikhin, M. A., & Titova, E. E. (2017). A contribution to the theory of the equatorial noise generation in the Earth's magnetosphere. *Geomagnetism and Aeronomy*, *57*(6), 691–697.

Shklyar, D. R., Parrot, M., Chum, J., Santolik, O., & Titova, E. E. (2010). On the origin of lower- and upper-frequency cutoffs on wedge-like spectrogram. *Journal of Geophysical Research*, *115*, A05203. https://doi.org/10.1029/2009JA014672

Smith, R. L., Brice, N. M., Katsufrakis, J., Gnrnett, D. A., Shawan, S. D., Belrose, J. S., & Barrington, R. E. (1964). An ion gyrofrequency phenomenon observed in satellites. *Nature*, *204*(4955), 274–275.

Storey, L. R. O. (1953). An investigation of whistling atmospherics. *Philosophical Transactions of the Royal Society*, *246*, 113–141.

Vavilov, D. I., & Shklyar, D. R. (2014). Ionospherically reflected proton whistlers. *Journal of Geophysical Research: Space Physics*, *119*, 9978–9991. https://doi.org/10.1002/2014JA020510